



**HAL**  
open science

## Light trapping in ZnO nanowire arrays covered with an absorbing shell for solar cells

Jérôme Michallon, Davide Bucci, Alain Morand, Mauro Zanucoli, Vincent Consonni, Anne Kaminski-Cachopo

► **To cite this version:**

Jérôme Michallon, Davide Bucci, Alain Morand, Mauro Zanucoli, Vincent Consonni, et al.. Light trapping in ZnO nanowire arrays covered with an absorbing shell for solar cells. *Optics Express*, 2014, 22 (S4), pp.A1174-A1189. 10.1364/OE.22.0A1174. hal-01112082

**HAL Id: hal-01112082**

**<https://hal.univ-grenoble-alpes.fr/hal-01112082>**

Submitted on 17 Jul 2019

**HAL** is a multi-disciplinary open access archive for the deposit and dissemination of scientific research documents, whether they are published or not. The documents may come from teaching and research institutions in France or abroad, or from public or private research centers.

L'archive ouverte pluridisciplinaire **HAL**, est destinée au dépôt et à la diffusion de documents scientifiques de niveau recherche, publiés ou non, émanant des établissements d'enseignement et de recherche français ou étrangers, des laboratoires publics ou privés.

# Light trapping in ZnO nanowire arrays covered with an absorbing shell for solar cells

Jérôme Michallon,<sup>1,2,3,\*</sup> Davide Bucci,<sup>1</sup> Alain Morand,<sup>1</sup> Mauro Zanucoli,<sup>4</sup> Vincent Consonni,<sup>2,3</sup> and Anne Kaminski-Cachopo<sup>1</sup>

<sup>1</sup>*Institut de Microélectronique Electromagnétisme et Photonique - Laboratoire d'Hyperfréquences et de Caractérisation (IMEP-LAHC), Grenoble INP Minatec, 3 parvis Louis Néel, CS 50257, 38016 Grenoble, France*

<sup>2</sup>*Univ. Grenoble Alpes, LMGP, F-38000 Grenoble, France*

<sup>3</sup>*CNRS, LMGP, F-38000 Grenoble, France*

<sup>4</sup>*Advanced Research Center on Electronic Systems for Information and Communication Technologies E. De Castro (ARCES) - Department of Electrical, Electronic and Information Engineering "Guglielmo Marconi" (DEI), University of Bologna, 47512 Cesena (FC), Italy*

\**Jerome.michallon@minatec.inpg.fr*

**Abstract:** The absorption properties of ZnO nanowire arrays covered with a semiconducting absorbing shell for extremely thin absorber solar cells are theoretically investigated by optical computations of the ideal short-circuit current density with three-dimensional rigorous coupled wave analysis. The effects of nanowire geometrical dimensions on the light trapping and absorption properties are reported through a comprehensive optical mode analysis. It is shown that the high absorptance of these heterostructures is driven by two different regimes originating from the combination of individual nanowire effects and nanowire arrangement effects. In the short wavelength regime, the absorptance is likely dominated by optical modes efficiently coupled with the incident light and interacting with the nearby nanowires (i.e. diffraction), induced by the period of core shell ZnO nanowire arrays. In contrast, in the long wavelength regime, the absorptance is governed by key optically guided modes, related to the diameter of individual core shell ZnO nanowires.

---

## References and links

1. J. A. Czaban, D. A. Thompson, and R. R. LaPierre, "GaAs core-shell nanowires for photovoltaic applications," *Nano Lett.* **9**(1), 148–154 (2009).
2. O. Gunawan and S. Guha, "Characteristics of vapor-liquid-solid grown silicon nanowire solar cells," *Sol. Energy Mater. Sol. Cells* **93**(8), 1388–1393 (2009).
3. G. Jia, M. Steglich, I. Sill, and F. Falk, "Core-shell heterojunction solar cells on silicon nanowire arrays," *Sol. Energy Mater. Sol. Cells* **96**, 226–230 (2012).
4. B. O'Donnell, L. Yu, M. Foldyna, and P. Roca i Cabarrocas, "Silicon nanowire solar cells grown by PECVD," *J. Non-Cryst. Solids* **358**(17), 2299–2302 (2012).
5. E. Garnett and P. Yang, "Light trapping in silicon nanowire solar cells," *Nano Lett.* **10**(3), 1082–1087 (2010).
6. J. Wang, Z. Li, N. Singh, and S. Lee, "Highly-ordered vertical Si nanowire/nanowall decorated solar cells," *Opt. Express* **19**(23), 23078–23084 (2011).
7. J. Li, H. Yu, and Y. Li, "Solar energy harnessing in hexagonally arranged Si nanowire arrays and effects of array symmetry on optical characteristics," *Nanotechnology* **23**(19), 194010 (2012).
8. K. E. Plass, M. A. Filler, J. M. Spurgeon, B. M. Kayes, S. Maldonado, B. S. Brunschwig, H. A. Atwater, and N. S. Lewis, "Flexible polymer-embedded Si wire arrays," *Adv. Mater.* **21**(3), 325–328 (2009).
9. M. C. Putnam, S. W. Boettcher, M. D. Kelzenberg, D. B. Turner-Evans, J. M. Spurgeon, E. L. Warren, R. M. Briggs, N. S. Lewis, and H. A. Atwater, "Si microwire-array solar cells," *Energy Environ. Sci.* **3**(8), 1037–1041 (2010).
10. J. Wallentin, N. Anttu, D. Asoli, M. Huffman, I. Aberg, M. H. Magnusson, G. Siefer, P. Fuss-Kailuweit, F. Dimroth, B. Witzigmann, H. Q. Xu, L. Samuelson, K. Deppert, and M. T. Borgström, "InP nanowire array solar cells achieving 13.8% efficiency by exceeding the ray optics limit," *Science* **339**(6123), 1057–1060 (2013).
11. C. Lévy-Clément, A. Katty, S. Bastide, F. Zenia, I. Mora, and V. Munoz-Sanjose, "A new CdTe/ZnO columnar composite film for Eta-solar cells," *Phys. E* **14**(1–2), 229–232 (2002).

12. C. Lévy-Clément, R. Tena-Zaera, M. Ryan, A. Katty, and G. Hodes, "CdSe-sensitized p-CuSCN/nanowire n-ZnO heterojunctions," *Adv. Mater.* **17**(12), 1512–1515 (2005).
13. R. Tena-Zaera, A. Katty, S. Bastide, C. Lévy-Clément, B. O'Regan, and V. Munoz-Sanjósé, "ZnO/CdTe/CuSCN, a promising heterostructure to act as inorganic eta-solar cell," *Thin Solid Films* **483**(1–2), 372–377 (2005).
14. R. Salazar, A. Delamoreanu, C. Levy-Clement, and V. Ivanova, "ZnO/CdTe and ZnO/CdS core-shell nanowire arrays for extremely thin absorber solar cells," *Energy Procedia* **10**, 122–127 (2011).
15. S. Sanchez, D. Aldakov, D. Rouchon, L. Rapenne, A. Delamoreanu, C. Lévy-Clément, and V. Ivanova, "Sensitization of ZnO nanowire arrays with CuInS<sub>2</sub> for extremely thin absorber solar cells," *J. Renew. Sustain. Energy* **5**(1), 011207 (2013).
16. V. Consonni, G. Rey, J. Bonaime, N. Karst, B. Doisneau, H. Roussel, S. Renet, and D. Bellet, "Synthesis and physical properties of ZnO/CdTe core shell nanowires grown by low-cost deposition methods," *Appl. Phys. Lett.* **98**(11), 111906 (2011).
17. H. Chao, J. Cheng, J. Lu, Y. Chang, C. Cheng, and C. Chen, "Growth and characterization of type-II ZnO/ZnTe core-shell nanowire arrays for solar cell applications," *Superlattices Microstruct.* **47**(1), 160–164 (2010).
18. J. Xu, X. Yang, H. Wang, X. Chen, C. Luan, Z. Xu, Z. Lu, V. A. L. Roy, W. Zhang, and C. S. Lee, "Arrays of ZnO/Zn<sub>x</sub>Cd<sub>1-x</sub>Se nanocables: band gap engineering and photovoltaic applications," *Nano Lett.* **11**(10), 4138–4143 (2011).
19. X. Wang, H. Zhu, Y. Xu, H. Wang, Y. Tao, S. Hark, X. Xiao, and Q. Li, "Aligned ZnO/CdTe core-shell nanocable arrays on indium tin oxide: synthesis and photoelectrochemical properties," *ACS Nano* **4**(6), 3302–3308 (2010).
20. J. Michallon, M. Zanucoli, A. Kaminski-Cachopo, V. Consonni, A. Morand, D. Bucci, F. Emieux, H. Szambolics, S. Perraud, and I. Semenikhin, "Comparison of optical properties of Si and ZnO/CdTe core/shell nanowire arrays," *Mater. Sci. Eng. B* **178**(9), 665–669 (2013).
21. K. Seo, M. Wober, P. Steinvurzel, E. Schonbrun, Y. Dan, T. Ellenbogen, and K. B. Crozier, "Multicolored vertical silicon nanowires," *Nano Lett.* **11**(4), 1851–1856 (2011).
22. S. Adachi, T. Kimura, and N. Suzuki, "Optical properties of CdTe: Experiment and modeling," *J. Appl. Phys.* **74**(5), 3435–3441 (1993).
23. G. Rey, D. Kohen, M. Modreanu, V. Consonni, C. Ternon, and D. Bellet, "Extraction of thin film refractive index from transmittance and reflectance spectra using a graphical inversion method," Submitted.
24. M. G. Moharam, E. B. Grann, D. A. Pommet, and T. K. Gaylord, "Formulation for stable and efficient implementation of the rigorous coupled-wave analysis of binary gratings," *J. Opt. Soc. Am. A* **12**(5), 1068–1076 (1995).
25. L. Li, "New formulation of the Fourier modal method for crossed surface-relief gratings," *J. Opt. Soc. Am. A* **14**(10), 2758–2767 (1997).
26. D. Bucci, B. Martin, and A. Morand, "Study of propagation modes of bent waveguides and micro-ring resonators by means of the aperiodic Fourier modal method," *Proc. SPIE* **7597**, 75970U (2010).
27. D. Bucci, B. Martin, and A. Morand, "Application of the three-dimensional aperiodic Fourier modal method using arc elements in curvilinear coordinates," *J. Opt. Soc. Am. A* **29**(3), 367–373 (2012).
28. L. Li, "Formulation and comparison of two recursive matrix algorithms for modeling layered diffraction gratings," *J. Opt. Soc. Am. A* **13**(5), 1024–1035 (1996).
29. J. Bischoff, "Formulation of the normal vector RCWA for symmetric crossed gratings in symmetric mountings," *J. Opt. Soc. Am. A* **27**(5), 1024–1031 (2010).
30. ASTM, Reference Solar Spectral Irradiance: Air Mass 1.5 spectra, <http://rredc.nrel.gov/solar/spectra/am1.5>, last accessed 15/07/2013.
31. B. C. P. Sturmberg, K. B. Dossou, L. C. Botten, A. A. Asatryan, C. G. Poulton, C. M. de Sterke, and R. C. McPhedran, "Modal analysis of enhanced absorption in silicon nanowire arrays," *Opt. Express* **19**(S5), A1067–A1081 (2011).
32. L. Wen, X. Li, Z. Zhao, S. Bu, X. Zeng, J. H. Huang, and Y. Wang, "Theoretical consideration of III-V nanowire/Si triple-junction solar cells," *Nanotechnology* **23**(50), 505202 (2012).
33. M. D. Kelzenberg, M. C. Putnam, D. B. Turner-Evans, N. S. Lewis, and H. A. Atwater, "Predicted efficiency of Si wire array solar cells," in *34th IEEE Photovolt. Specialists Conf.* (2009), pp. 001948–001953.
34. M. Zanucoli, J. Michallon, I. Semenikhin, C. Fiegna, A. Kaminski-Cachopo, E. Sangiorgi, and V. Vyrkov, "Numerical simulation of vertical silicon nanowires based heterojunction solar cells," *Energy Procedia* **38**, 216–222 (2013).
35. A. Snyder and J. Love, *Optical Waveguide Theory* (Springer, 1983).
36. L. Li, "Use of Fourier series in the analysis of discontinuous periodic structures," *J. Opt. Soc. Am. A* **13**(9), 1870–1876 (1996).

---

## 1. Introduction

Over the last decade, increasing interest has been devoted to core shell nanowire (NW)-based solar cells [1–4] due to their ability to achieve high absorption and low-reflection, as well as to efficiently separate and collect photo-generated charge carriers. Core shell NW arrays are able to efficiently trap light [5–7], which in turn enhances their absorption properties. Additionally, when the NW radius is much smaller than the diffusion length, photo-generated

charge carriers may efficiently be separated over a short distance and collected in the electrodes owing to the very high NW crystalline quality. Accordingly, core shell NW-based solar cells may be considered as a good alternative to planar layer based-solar cells, especially for mobile or flexible devices on polymer substrates [8]. Photoconversion efficiencies as high as 7.9 [9] and 13.8% [10] have for instance been reported for core shell Si and InP NW arrays, respectively.

More recently, solar cells based on ZnO NW arrays have attracted much attention due to the ability of ZnO to grow as nanostructures with a wide variety of low-cost chemical deposition techniques such as electro-deposition [11–15], chemical bath deposition [16], or chemical vapor deposition [17]. However, ZnO NWs do not significantly contribute to the absorption owing to its wide band gap energy of 3.3 eV at room temperature. When ZnO NW arrays are covered with an extremely thin absorber (ETA) semiconducting absorbing shell, the so-called ETA solar cells based on core shell ZnO NW heterostructures can reach photoconversion efficiency as high as 4.74% [18]. CuInS<sub>2</sub> (CIS) or II-VI compound semiconductors have emerged as potential semiconducting absorbing shells: CdTe [11, 13, 14, 16, 19], CdSe [12, 18] CIS [15], CdS [14] or ZnTe [17] can usually be deposited by electrodeposition [12, 19], vapor phase epitaxy [11], close space sublimation [16], successive ionic layer adsorption and reaction [14, 15], metal organic chemical vapor deposition [13, 17] or wet chemistry [18]. Furthermore, the type II band alignment between ZnO NWs and the semiconducting absorbing shell is also expected to efficiently separate photo-generated charge carriers without any required doping.

Importantly, the light trapping and absorption properties are strongly dependent upon the geometrical dimensions of ZnO NW arrays covered with the semiconducting absorbing shell, which should therefore be controlled and optimized. It has been shown that 1  $\mu\text{m}$ -long ZnO NW arrays covered with CdTe semiconducting absorbing shells more efficiently absorb light than both 1  $\mu\text{m}$ -long Si NW arrays and ZnO/CdTe planar layers with the same amount of materials [20].

The optical design of core shell ZnO NW heterostructures should be assisted by a physical insight into the light trapping process and not only by brute-force numerical calculations. The clear understanding of the absorption phenomena is crucial to determine the proper sizing of highly efficient ZnO NW arrays covered with semiconducting absorbing shells. Interestingly, it has recently been shown that the guided modes play an important role on the optical properties of Si NW arrays [21]. The contribution of the propagation modes to the absorptance of the structure is thus investigated hereafter by three-dimensional (3D) rigorous coupled wave analysis (RCWA) in order to elucidate the physical mechanisms responsible for light absorption. First, the geometry of core shell ZnO NW heterostructures is described together with the optical simulation methodology. Then, two representative sets of NW geometrical dimensions are studied in details following the maps of the ideal short circuit current density. The first set of geometrical dimensions with a constant diameter of 200 nm and a varying period is investigated in order to study individual NW effects through single optically guided modes and NW arrangement effects through diffraction processes. Finally, the second set of geometrical dimensions with a constant period and a varying diameter is used to analyze the absorption of single and multi optically guided mode configurations.

## 2. Methods

### 2.1. Investigated structures

The structural morphology of the investigated ZnO/CdTe core shell NW arrays distributed in a square geometrical configuration is presented in Fig. 1. The ZnO/CdTe NW height and CdTe thickness are 1  $\mu\text{m}$  and 40 nm, respectively. The diameter ( $D$ ) refers to the total diameter of ZnO/CdTe core shell NWs while the NW array period ( $P$ ) is defined as the distance between the centers of two nearby ZnO NWs. The calculations of the ideal short circuit current density ( $J_{\text{sc}}$ ) were achieved on ZnO/CdTe core shell NW arrays deposited on fluorine-doped tin oxide (FTO) on glass substrates as depicted in Fig. 1(a). The ZnO seed

layer in between the ZnO/CdTe core shell NW arrays and FTO/glass substrate is required to induce the formation of ZnO NWs. The FTO and ZnO seed layer thicknesses were taken as 300 and 20 nm, respectively. The optical mode analysis was performed on semi-infinite ZnO/CdTe core shell NW arrays in order to avoid the influence of the light reflected by the substrate, as depicted in Fig. 1(b). Each ZnO/CdTe core shell NW was divided into two parts: the shell on top of the NW is referred as the CdTe cap while the two concentric cylinders of ZnO and CdTe are referred as the ZnO/CdTe nano-fibre, as presented in Fig. 1(b). The absorptance of semi-infinite ZnO/CdTe core shell NW arrays was calculated either in the ZnO/CdTe nano-fibre or in both the ZnO/CdTe nano-fibre and CdTe cap. The optical databases were taken from Refs [20, 22, and 23] for ZnO, CdTe and FTO.

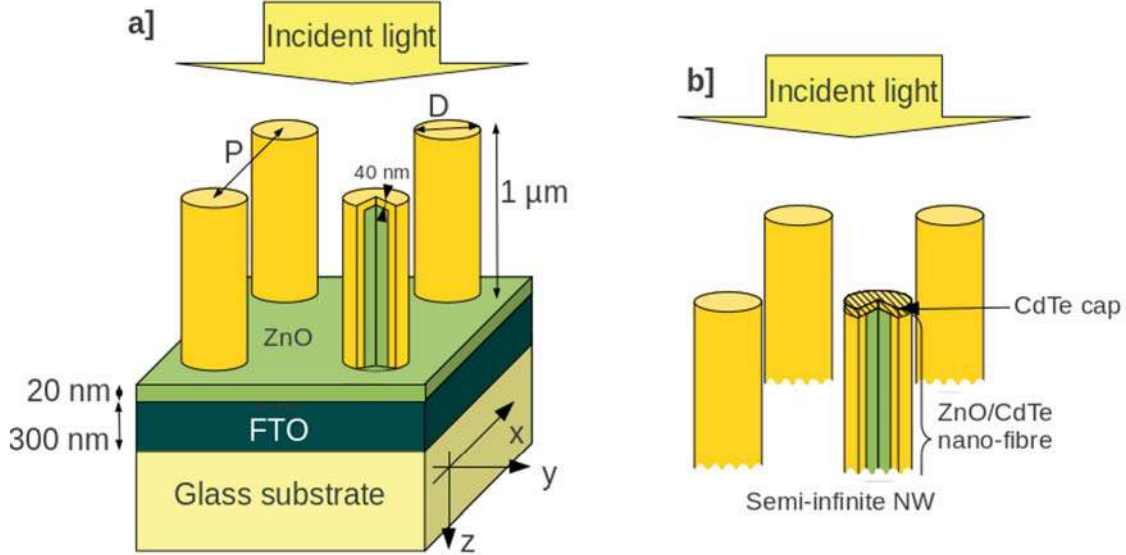


Fig. 1. Schematic view of (a) the ZnO/CdTe core shell NW arrays on FTO/glass substrate and of (b) semi-infinite NW arrays for the optical mode analysis.

## 2.2. Optical simulation principles

The optical simulations were performed by 3D RCWA [24, 25], with a home-made software developed at IMEP-LAHC laboratory [26, 27]. In the framework of RCWA, the propagating light wavelength is selected at the very beginning of the simulation. The simulated structure is represented by a stack of different layers: the cross-section is perpendicular to the propagation axis ( $z$ ) and invariant inside each layer. According to the representation with a truncated Fourier series of different parameters such as the refractive index cross sections, electric and magnetic fields, Maxwell equations are solved by mean of algebraic matrix calculations. In particular, the propagation modes are calculated separately for each layer via eigenvalues and eigenvectors. Then, the total field continuity is imposed at each interface separating two consecutive layers using a scattering matrix approach [28]. At the end of the simulation, the propagation modes of each layer with their associated propagation constants and excitation coefficients are determined. For instance, the  $x$ -component of the electric field of a propagating mode ( $E_x^{\text{mode}}$ ) can be expressed as:

$$E_x^{\text{mode}} = C(x, y) \cdot \exp(j \cdot \omega \cdot t) \cdot \exp(-j \cdot \beta \cdot z), \quad (1)$$

where  $C(x, y)$  is the spatial cross-section distribution of the mode in the  $x$ - $y$  plane,  $\omega$  is the radial frequency,  $t$  is the time,  $\lambda$  is the incident wavelength,  $\beta$  is the complex propagation constant (i.e.  $\beta = \beta_r - j\beta_i$ ).

The light propagating in the structure described by the total electric and magnetic fields is computed by summing all the modal contributions. Each modal contribution corresponds to modes propagating similarly to those in optical fibers. If a polychromatic light is propagated, the polychromatic spectrum is discretized and the optical simulation steps described above are repeated for each wavelength.

Since the investigated structure is symmetric, the truncated Fourier series were written with only 10x10 positive harmonics along the  $x$ - and  $y$ -direction (see Appendix A). This

allows a decrease in the matrix size by a factor of 4 and correlatively in the computation time by a factor of about 25 [29]. As a result, the calculated spatial  $x$ - $y$   $E_x^{\text{mode}}$  map presents symmetric profiles. The structure was excited with a symmetric incident plane wave propagating along the  $z$ -direction and polarized with the electric field parallel to the  $x$ -direction. The incident plane wave can thus be coupled to the calculated modes since they both share symmetric profiles.

The Poynting vector was calculated from the electric and magnetic fields. The reflectance ( $R$ ) and transmittance ( $T$ ) were computed from the integration of the Poynting vector over two  $x$ - $y$  planes (before and after the NW array layer). The absorptance ( $A$ ) was then derived from:

$$A(\lambda) = 1 - R(\lambda) - T(\lambda), \quad (2)$$

By assuming that each of the photo-generated electron-hole pair is collected by the electrodes, the ideal short-circuit current density is given by:

$$J_{\text{sc}} = \frac{q}{hc} \int A(\lambda) I_{\text{AM1.5g}}(\lambda) \lambda d\lambda, \quad (3)$$

where  $q$ ,  $h$  and  $c$  are the electron charge, Planck constant and light velocity, respectively.  $I_{\text{AM1.5g}}$  is the ASTM AM1.5G solar irradiance taken from Ref. [30]. Due to the negligible solar irradiance below  $\lambda = 300$  nm and to the CdTe band gap energy of 1.5 eV, Eq. (3) was numerically calculated in the wavelength range of 300-830 nm.  $D$  as well as  $P$  were varied in order to find the geometrical dimensions leading to the largest ideal  $J_{\text{sc}}$ .

### 2.3. Optical mode analysis

Once the geometrical dimensions of ZnO/CdTe core shell NW arrays were optimized by varying  $D$  and the  $D/P$  ratio as seen in Fig. 2(a) [20], the physical mechanisms responsible for light absorption were investigated *via* an optical mode analysis. Three types of optical modes propagating along  $z$  occur in any waveguides such as optical fibre or NW arrays: guided, radiated and evanescent modes. The electric and magnetic fields of guided modes are confined in the ZnO/CdTe core shell NW similarly to the optically guided modes used to convey information in optical fibres. In contrast, the electric and magnetic fields of radiated modes are mainly propagating outside the ZnO/CdTe core shell NW. The electric and magnetic fields of evanescent modes exponentially decay in the propagation direction  $z$ . In contrast to the radiated and evanescent modes, the number of optically guided modes is finite. Here, the relevance of guided modes for the overall absorptance of NW arrays is thus investigated for wavelength ranging from 430 to 830 nm. The guided modes are characterised by a real part of their normalized propagation constant such as  $1 < \beta_r \lambda / 2\pi < n_{\text{CdTe}} < n_{\text{ZnO}}$ . The guided modes are also characterized by a relatively small imaginary part of the propagation constant related to the absorption.

Three types of physical quantities were computed to characterise optically guided modes: the electric field distribution factors, coupling factor and absorptance (details of calculation are given in appendix B).

According to Maxwell's continuity equations, the  $x$ -component of the electric field ( $E_x$ ) is continuous (resp. discontinuous) along the  $y$ -direction (resp.  $x$ -direction) crossing the NW centre. Two distinct distributions of the electric field amplitude ( $E$ ) are thus obtained along the  $x$ - and  $y$ -directions. By performing the 1D integration of the spatial  $x$ - $y$   $E$  maps along these  $x$ - and  $y$ -directions, the  $x$ - and  $y$ -electric field distribution factors ( $\rho_x$  and  $\rho_y$ ) were computed as follows:

$$\rho_x = \frac{\int_{\text{CdTe}} |E(x, y)|^2 dx}{\int_{\text{all}} |E(x, y)|^2 dx} \Bigg|_{y=\text{middle}}, \quad \rho_y = \frac{\int_{\text{CdTe}} |E(x, y)|^2 dy}{\int_{\text{all}} |E(x, y)|^2 dy} \Bigg|_{x=\text{middle}}, \quad (4)$$

$\rho_x$  and  $\rho_y$  give an indication of the electric field confinement in the CdTe shell for two extreme polarisation states with either the exciting electric field parallel or perpendicular to the NW interface, respectively. They are thus a good metric for quantifying the electric field distribution in the NW under solar illumination with all kinds of polarisation.

The coupling factor (i.e., mode excitation coefficient), computed for each optically guided mode, measures the coupling between the ZnO/CdTe nano-fibre array and the incident plane-wave. Basically, the light is initially transmitted through the CdTe cap and then through the ZnO/CdTe nano-fibre (see Fig. 1(b)). In other words, the ability of the optically guided mode to be excited and so to propagate its energy is quantified by the coupling factor.

The specific optically guided modes with an absorptance larger than 1% are referred as key optically guided modes [31, 32]. Two important criteria are required for an efficient absorption of the incident light by these key optically guided modes: (1) their coupling factor must be large, (2) the mode must be mainly confined in the CdTe shell with large  $\rho_x$  and  $\rho_y$ .

#### 2.4. Generation rate calculations

The generation rate ( $G$ ) represents the number of photo-generated carriers per unit volume and unit time and was calculated from the electric field as follows [33]:

$$G(x, y, z, \lambda) = \frac{\pi \cdot \Im[\varepsilon(x, y, z, \lambda)] \cdot |E(x, y, z, \lambda)|^2}{h}, \quad (5)$$

where  $\varepsilon$  and  $E$  are the permittivity and the electric field, respectively.

The generation rate maps are used to analyze the spatial distribution of photo-generated charge carriers. By assuming that the 3D generation rate presents a radial symmetry in the NW, the radial  $r$ - $z$  generation rate can be computed by averaging the 3D generation rate over a circle perimeter, following the method of Ref [33]. More details are given in appendix C.

### 3. Results and discussion

The map of the ideal  $J_{sc}$  is computed with Eq. (3) and reported in Fig. 2(a) as a function of  $P$  and  $D/P$ . The largest ideal  $J_{sc}$  is reached for  $P = 350$  nm and  $D = 200$  nm, which are consequently referred hereafter as the optimal geometrical dimensions. The variation of the ideal  $J_{sc}$  is small: the ideal  $J_{sc}$  decreases by only 2% while varying  $P$  and  $D$  in the range of 300-400 nm and 180-280 nm, respectively.

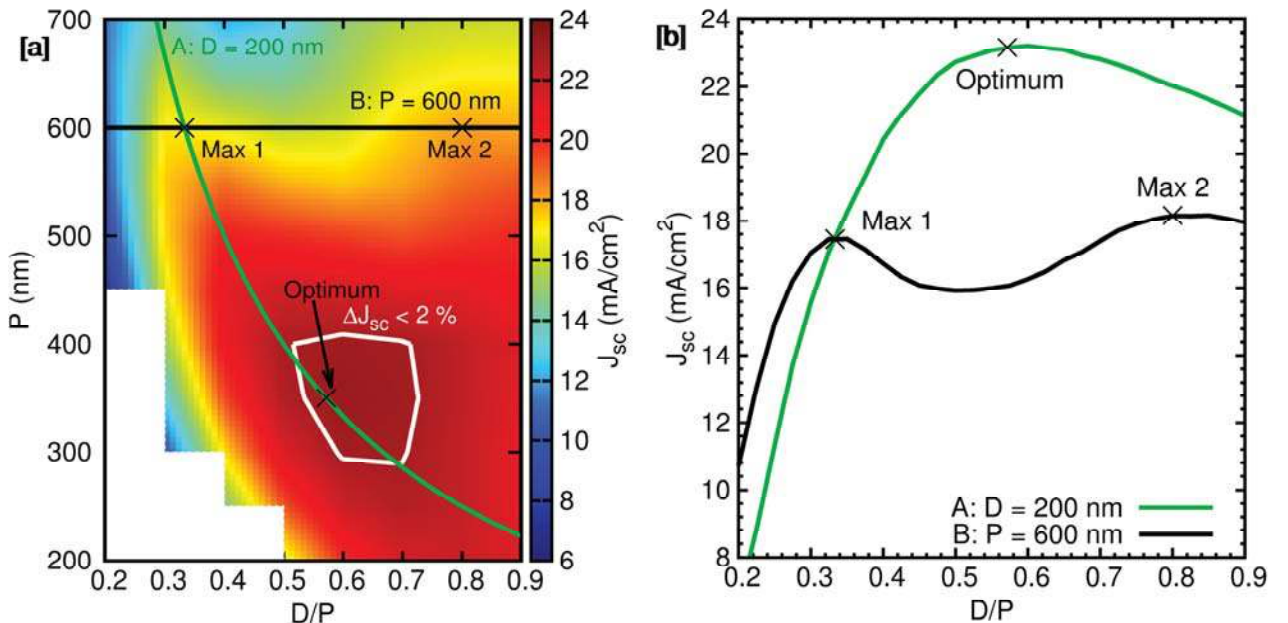


Fig. 2. (a) Ideal  $J_{sc}$  map as a function of  $P$  and  $D/P$ . (b) Ideal  $J_{sc}$  as a function of  $D/P$  for the two sets of geometrical dimensions A and B.

For  $P > 500$  nm, two local maxima arise in the ideal  $J_{sc}$  map as a function of  $D/P$ . Accordingly, two sets of geometrical dimensions are studied in detail in the following, in order to elucidate the absorption mechanisms:

- The set of dimensions A:  $D$  is kept constant at 200 nm whereas  $P$  is varied. As seen in Fig. 2(b), one maximum is revealed and corresponds to the optimal geometrical dimensions. The set of geometrical dimensions A is thus investigated, in order to study the contribution of a single key optically guided mode (with  $D = 200$  nm) and the diffraction processes ( $P$  is varied).
- The set of dimensions B:  $P$  is kept constant at 600 nm while  $D$  is varied. Two local maxima are obtained for  $D = 200$  nm (i.e., Max 1) and  $D = 480$  nm (i.e., Max 2), as shown in Fig. 2(b). The set of dimensions B is used to compare the absorptance of individual NW with single and multi optically guided key mode configurations.

### 3.1. Set of geometrical dimensions A: $D = 200$ nm, varying $P$

#### 3.1.1. Absorptance spectra for various periods

The absorptance versus wavelength of the complete structure with ZnO/CdTe core shell NW arrays deposited on FTO/glass substrate (sketched in Fig. 1(a)) is presented in Fig. 3(a). An absorptance of about 90% (resp. 50%) for the geometrical dimension corresponding to the optimum (resp. Max 1) is revealed. Interestingly, the absorptance of the arrays comprising both the ZnO/CdTe nano-fibre and CdTe cap (depicted in Fig. 1(b)) follows the absorptance of the complete structure. Since the only distinction between the two structures is the presence of the ZnO/FTO/glass substrate below the ZnO/CdTe core shell NW arrays, the difference of absorptance is ascribed to the light reflected by the substrate. The weak absorptance improvement of less than 10% when ZnO/FTO/glass substrate is used reveals that the light is mostly absorbed during the first propagation through the ZnO/CdTe core shell NWs and that the substrate has a limited effect on the absorption. The absorption mechanism of the ZnO/CdTe NW arrays is thus investigated in more details hereafter by computing the absorptance of the optical modes for the semi-infinite nano-fibre. The absorption enhancement, as observed in Fig. 3(a), through resonant peaks is due to weak Fabry-Perot resonances between the top and bottom of ZnO/CdTe core shell NWs. This appears as a remarkable difference with the absorption of NWs made of indirect band gap semiconductors such as Si, where strong Fabry-Perot resonances strongly operate between the top and bottom of NWs and govern the absorptance [31, 34].

Moreover, the absorptance versus wavelength is reported in Fig. 3(b) for  $D = 200$  nm and various  $P$  (i.e. the set of geometrical dimensions A). In the short wavelength regime (i.e.,  $\lambda < 550$  nm), the absorptance increases as  $P$  is decreased and reaches about 85% for  $P$  ranging from 250 to 350 nm. The significant absorptance suggests that diffraction process occurs as  $P$  is comparable to the wavelength.

In contrast, an absorptance peak arises in the long wavelength regime (i.e.,  $\lambda > 700$  nm) and is relatively independent upon  $P$  for  $P > 500$  nm: the maximum absorptance peak is changed by less than 4% while the wavelength corresponding to the maximum absorptance is shifted by less than 40 nm. As  $P$  is increased, the optical interaction between the NWs decreases since the NWs are farther from each other. Individual NW effects thus drive the absorption. For  $P = 600$  nm, the observed peak at  $\lambda > 700$  nm therefore originates likely from individual NW effects. In order to support this assumption, an optical mode analysis is performed for the optimal geometrical dimensions (i.e.,  $D = 200$  nm and  $P = 350$  nm).

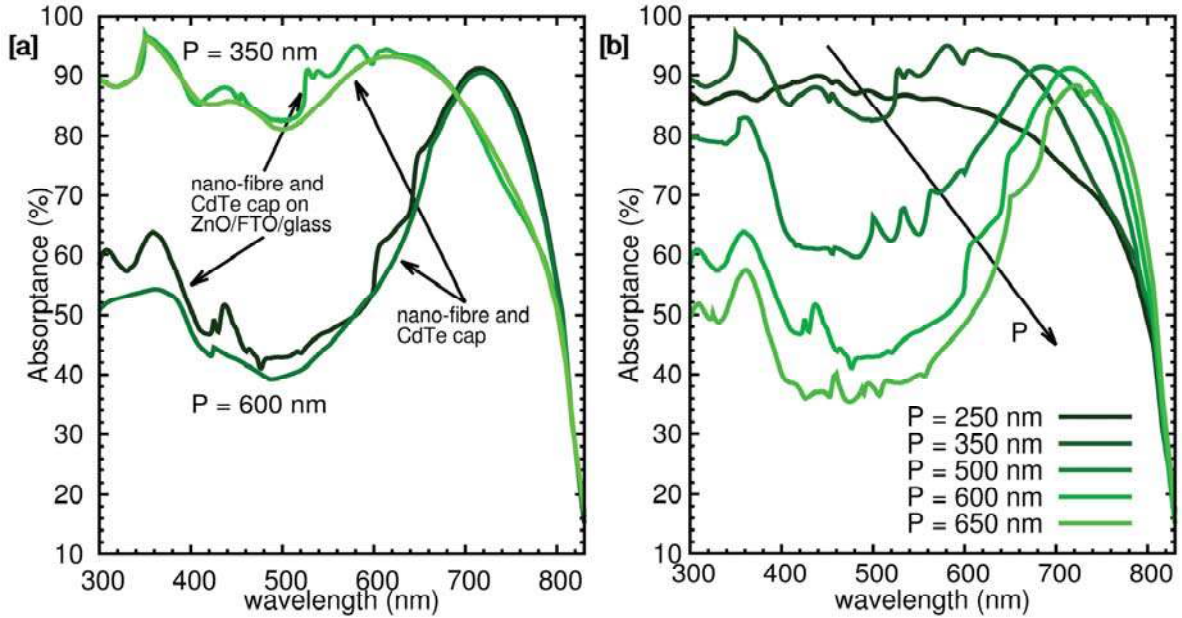


Fig. 3. Absorbance characteristics for ZnO/CdTe core shell NW arrays with  $D = 200$  nm and various periods (i.e., set of geometrical dimensions  $A$ ).

### 3.1.2. Optimal geometrical dimensions

#### 3.1.2.1. Optical mode investigation

The real part of the propagation constant and the absorbance of 5 selected optical modes, computed for the semi-infinite nano-fibre, are reported in Figs. 4(a) and 4(b). The normalized propagation constant (i.e.,  $\beta_r \lambda / 2\pi$ ) for the optical mode 1 (resp. 2) first increases from 1.6 (resp. 1.3) at  $\lambda = 300$  nm to 2.5 (resp. 1.5) at  $\lambda = 380$  nm and subsequently decreases to 1.42 (resp. 1.38) at  $\lambda = 830$  nm. Optical mode 1 and 2 are thus by definition pure optically guided modes since  $\beta_r \lambda / 2\pi$  is in between the air and CdTe refractive indices. For  $\lambda > 430$  nm, the calculated absorbance of the optically guided mode 1 is larger than 20 % as reported in Fig. 4(b) while the calculated absorbance of the key optically guided mode 2 is lower than 0.003 %, regardless of the wavelength. The optically guided mode 2 is thus not a key mode by definition. The optically guided mode 1 is the only one key mode. The large absorbance peak around  $\lambda = 700$  nm of the key optically guided mode corresponds to the large absorbance of ZnO/CdTe core shell NW arrays for large  $P$  (see Fig. 3(b)). The key optically guided mode thus predominantly contributes to the absorption in the long wavelength regime, as previously assumed.

The propagation constant of the optical mode 3 (resp. 4) decreases from  $\beta_r \lambda / 2\pi$  of about 2 (resp.  $\beta_r \lambda / 2\pi = 1.03$ ) at  $\lambda = 300$  nm to  $\beta_r \lambda / 2\pi = 1$  at  $\lambda = 430$  nm, indicating that the modes are optically guided in this range of wavelength. For longer  $\lambda$ , both optical modes become radiated modes with the propagation constants decreasing until reaching 0.01 at  $\lambda = 600$  nm and 830 nm for the optical mode 3 and 4, respectively. In contrast, the optical mode 5 is a purely radiated mode with  $\beta_r \lambda / 2\pi$  decreasing from 0.62 at  $\lambda = 300$  nm to 0.01 at  $\lambda = 690$  nm. Interestingly, the  $x$ -component of the electrical field of the optical mode 4 is relevant outside of the ZnO/CdTe NW, as seen in Fig. 4(c). This suggests that the interactions with the nearby NWs are significant. Furthermore, the optical mode 4 is well coupled with the incident light since  $\beta_r \lambda / 2\pi$  is close to 1. When both coupling and NW arrangement effects become significant, the interaction of the incident light with the NW arrangement occur, which may results in diffraction processes. Both conditions are fulfilled for the optical mode 4, as seen in Figs. 4(a)–4(c). The absorbance of the optical mode 4 is thus large (i.e., around 40 %) from  $\lambda = 300$  nm to  $\lambda = 600$  nm and then decreases significantly, as visible in Fig. 4(b). The optical mode 3 (resp. 5) contributes to the absorbance for  $\lambda < 550$  nm (resp.  $\lambda < 430$  nm) with a value of about 7 % (resp. 15 %).

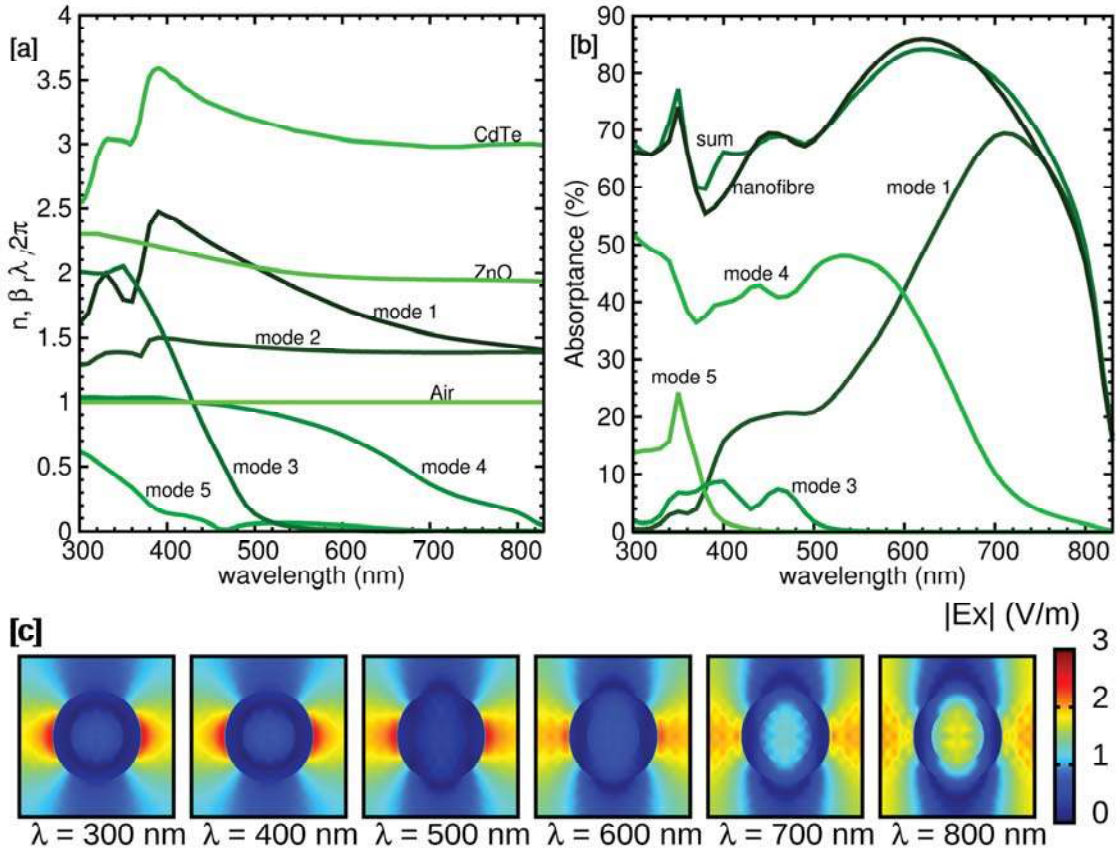


Fig. 4. (a) The real part of the normalized propagation constant (i.e.  $\beta_r \lambda / 2\pi$ ) and (b) the absorbance for the 5 selected optical modes found for the optimal geometrical dimensions with  $D = 200$  nm and  $P = 350$  nm. The real part of the refractive indices (i.e.  $n$ ) for ZnO and CdTe is also reported in (a) for comparison. (c) Maps of the modulus of the electric field  $E_x$  for the optical mode 4 for various wavelength

The sum of the absorbance of all 5 selected optical modes fits the absorbance of the ZnO/CdTe nano-fibre (sketched in Fig. 1(b)) calculated without taking into account the reflection with the substrate, as reported in Fig. 4(b). The small variation in between these two curves can arise from interference between modes. In other words, the phase difference between propagating modes is not taken into account with the summation of mode absorbances.

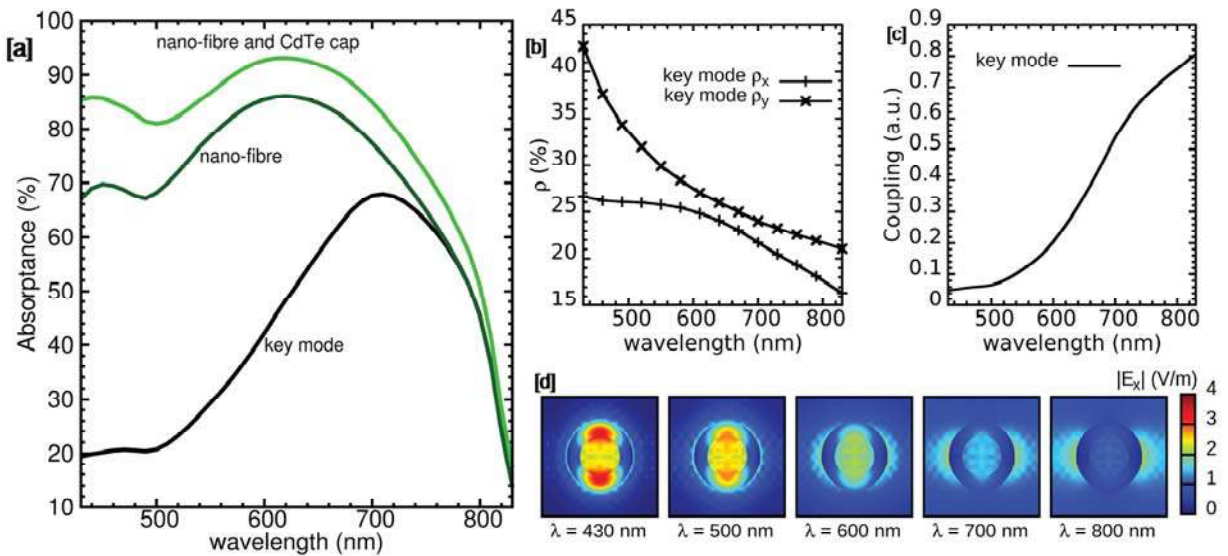


Fig. 5. Characteristics of the key optically guided mode found for the optimal geometrical dimensions with  $D = 200$  nm and  $P = 350$  nm. (a) Absorbance versus wavelength for the key optically guided mode, for the ZnO/CdTe nano-fibre array, for the array comprising both the ZnO/CdTe nano-fibre and the CdTe cap, and for the complete structure. (b) Electric field distribution factors  $\rho_x$  and  $\rho_y$  versus wavelength and (c) coupling factor of the key optically guided mode versus wavelength. (d) Maps of the modulus of the electric field  $E_x$  for the key optically guided mode represented for various wavelengths.

In the following, the key optically guided mode (i.e., optical mode 1) is studied in more details: the electric field distribution factors (i.e.,  $\rho_x$  and  $\rho_y$ , as defined in section 2.3) and the coupling factor are thus presented in Figs. 5(b) and 5(c). In Fig. 5(b),  $\rho_y$  decreases from 43% at  $\lambda = 430$  nm to 21% at  $\lambda = 830$  nm. A weaker confinement is found for  $\rho_x$  decreasing from 27% to 17% in the same wavelength range. Indeed, the  $x$ -component of the the electric field (i.e.,  $E_x$ ) is less confined in the CdTe shell as  $\lambda$  is increased: this is clearly shown in Fig. 5(d) where several  $|E_x|$  maps are reported for various wavelengths. This is confirmed in Fig. 4(a) by the decrease in the real part of the normalized propagation constant as  $\lambda$  is increased above 430 nm. The decrease in the electric field distribution factors is well-known for optical step-index fibres: basically, the confinement is larger for smaller wavelengths than for longer wavelengths [35]. However, since  $\rho_y$  is larger than 21% regardless of the wavelength, the key optically guided mode remains thus relatively well-confined in the CdTe shell. At smaller wavelengths (i.e., around  $\lambda = 430$  nm),  $E_x$  is concentrated within the ZnO/CdTe core shell NW, as shown in Fig. 5(d). This results in a larger real part of the normalized propagation constant (i.e.,  $\beta_r \lambda / 2\pi = 2.3$  in Fig. 4(a)). Therefore, the coupling of the key optically guided mode with the incident plane-wave is not efficient due to the propagation constant mismatch. As the wavelength is increased,  $E_x$  is less confined in the ZnO/CdTe core shell NW resulting in a smaller propagation constant (i.e.,  $\beta \lambda / 2\pi = 1.52$  at  $\lambda = 700$  nm and  $\beta \lambda / 2\pi = 1.42$  at  $\lambda = 800$  nm, for instance) accounting for the increase in the coupling factor above 0.5 at  $\lambda = 700$  nm (see Fig. 5(c)).

As stated before, both the electric field distribution and coupling factors must be large in order to get an efficient absorption. Although  $\rho_x$  and  $\rho_y$  decrease as wavelength is increased, while the coupling factor increases,  $\rho_x$  and  $\rho_y$  are still large in the long wavelength regime (i.e.,  $\lambda > 700$  nm). This results in a large absorptance peak of the key optically guided mode reaching its maximum of 68% at  $\lambda = 710$  nm.

The absorptance of the ZnO/CdTe nano-fibre calculated without taking into account the reflection with the substrate is larger than 80 and 66% with and without the CdTe cap, respectively (see Fig. 5(a)). In the long wavelength regime, the absorptance of the ZnO/CdTe nano-fibre with and without the CdTe cap is dominated by the absorptance related to the key optically guided mode. The absorption mechanism of ZnO/CdTe NW arrays should be distinguished from the absorption of planar layers, which is driven by the intrinsic material properties resulting in a poorer absorption at long wavelength. In the case of ZnO/CdTe NW arrays, the electric and magnetic fields are confined into the absorbing shell *via* the key optically guided mode, resulting in a more efficient absorption. Other highly absorbing direct band gap semiconductors such as CdSe, ZnTe, CdS or CIS are also expected to behave similarly to CdTe when associated with ZnO NW arrays.

### 3.1.2.2. Generation rate analysis

The previous optical mode analysis shows two regimes where individual NW effects and NW arrangement effects drive the absorptance. However, the analysis does not yield where the charge carriers are photo-generated, while this knowledge would be valuable for the complete understanding of ETA solar cells. The map of the generation rate represents the number of photo-generated carriers per unit volume and unit time at each spatial coordinate. The monochromatic and polychromatic radial generation rates are reported in Fig. 6 for the optimal geometrical dimensions (i.e.,  $D = 200$  nm and  $P = 350$  nm) following the calculations described in section 2.4.

In the linear colour scale of Fig. 6(a), it is revealed that the absorption at  $\lambda = 300$  nm is achieved in the few first nanometres of the CdTe cap, as in the case of planar layers. This is due to the small absorption depth of CdTe, the inverse of the Beer-Lambert absorption coefficient  $\alpha$  denoted  $\alpha^{-1}$  being 14 nm at  $\lambda = 300$  nm. Until  $\lambda = 400$  nm, the absorption of the CdTe cap is highly efficient since  $\alpha^{-1}$  is smaller than the CdTe thickness (i.e.,  $\alpha^{-1} = 33$  nm at  $\lambda = 400$  nm). This can also be seen in Fig. 5(a), by comparing the absorptance spectra of the ZnO/CdTe nano-fibre array and of the array with both the ZnO/CdTe nano-fibre and CdTe

cap. The absorptance of the CdTe cap is thus of about 20% at  $\lambda = 400$  nm. For  $\lambda > 500$  nm, the contribution of the CdTe cap is no longer significant (i.e., smaller than 10%, as presented in Fig. 5(a)) since  $\alpha^{-1}$  is larger than 90 nm. Therefore, the light is absorbed deeper in the CdTe absorbing shell of the ZnO/CdTe nano-fibre array, as shown in Fig. 6(b).

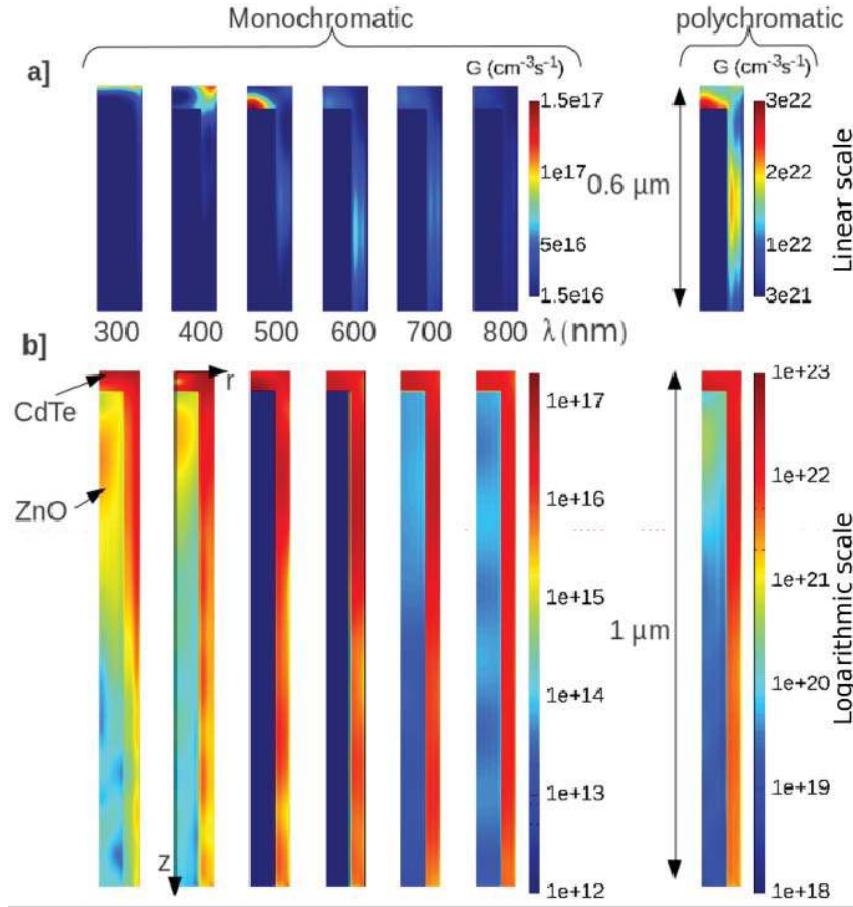


Fig. 6. Monochromatic and polychromatic radial generation rate maps in the ZnO/CdTe core shell NW calculated for the optimal geometrical dimensions with  $D = 200$  nm and  $P = 350$  nm. (a) Linear scale within the first 600 nm from the top of the CdTe cap and (b) logarithmic scale for the whole NW.

In summary, for the set of geometrical dimensions A, the absorption properties are driven by individual NW effects at the long wavelength regime (i.e.,  $\lambda > 700$  nm) *via* the key optically guided mode of the ZnO/CdTe nano-fibre. In contrast, optical modes interacting with the nearby NWs and coupled with the incident light (i.e., diffraction process) induced by NW arrangement effects are likely dominating the absorption in the short wavelength regime (i.e.,  $\lambda < 550$  nm), in particular for small  $P$ . The optimal geometrical dimensions (i.e.,  $D = 200$  nm and  $P = 350$  nm) are more likely due to a trade-off between an efficient diffraction process (coming from NW arrangement effects and related to  $P$ ) and the relatively large absorption of one key optically guided mode (originating from individual NW effects and related to  $D$ ). Fabry-Perot resonances are also contributing to the absorptance with a value smaller than 10%.

### 3.2. Set of geometrical dimensions B: $P = 600$ nm, varying $D$

#### 3.2.1. Optically guided mode investigations

The set of geometrical dimensions B with a large and constant  $P = 600$  nm is investigated in this section. The number of optical guided modes (i.e. having a propagation constant  $\beta$  for which  $1 < \beta\lambda / 2\pi < n_{\text{CdTe}} < n_{\text{ZnO}}$ ) and key modes (with an absorptance larger than 1%) is reported in Table 1 as a function of wavelength for several  $D$ . For a given wavelength, the number of guided modes increases with  $D$ , as commonly observed for step-index optical fibres [35]. For  $D$  ranging from 150 to 200 nm, two optically guided modes are determined

when  $\lambda$  is varied from 450 to 830 nm. However, only one of them fulfils the criterion of key optically guided modes. For the geometrical dimensions B with  $D = 480$  nm, the number of optically guided modes is of 14 for  $\lambda = 430$  nm and it decreases down to 5 at  $\lambda = 800$  nm as seen in Table 1. No more than four of them fulfil the criterion of key optically guided modes in the same wavelength range.

**Table 1. Number of optically guided modes (resp. key optically guided modes) obtained for different  $D$  and  $\lambda$ , for the set of geometrical dimensions B with  $P = 600$  nm.**

	$D$ (nm)	$\lambda$ (nm)				
		430	500	600	700	800
	150	2 (1)	2 (1)	2 (1)	2 (1)	2 (1)
	175	2 (1)	2 (1)	2 (1)	2 (1)	2 (1)
	200	3 (1)	2 (1)	2 (1)	2 (1)	2 (1)
	300	8 (3)	7 (3)	2 (1)	2 (1)	2 (1)
	400	14 (3)	7 (3)	7 (3)	2 (1)	2 (1)
	480	14 (4)	9 (4)	7 (4)	6 (4)	5 (2)
	550	17 (6)	9 (4)	7 (4)	7 (3)	6 (2)

The absorptance of the key optically guided mode 1 and of the ZnO/CdTe nano-fibre are presented in Fig. 7 for various  $D$ , in order to elucidate the origin of the two local maxima for the ideal  $J_{sc}$  as reported in Fig. 2(b).

In Fig. 7(a), the absorptance of single key optically guided mode configurations with  $D$  ranging from 150 to 200 nm is reported. It is worth noticing that the maximum of the absorptance of the key optically guided mode is red-shifted in the wavelength range of 640 to 750 nm when  $D$  increases. It is also seen in Fig. 7(a) that the absorptance of the key optically guided mode fits the absorptance of the ZnO/CdTe nano-fibre. Other optical modes such as radiative or evanescent modes that are not considered here, probably contribute to the absorption of the ZnO/CdTe nano-fibre, as shown for  $P = 350$  nm and  $D = 200$  nm. For  $D = 200$  nm (i.e., Max 1 in Fig. 2(b)), the absorptance peak of the ZnO/CdTe nano-fibre is broader as compared with  $D = 175$  nm. The geometrical dimensions with  $D = 200$  nm are thus more efficient as previously discussed for the set of geometrical dimensions A (see Fig. 2(b)).

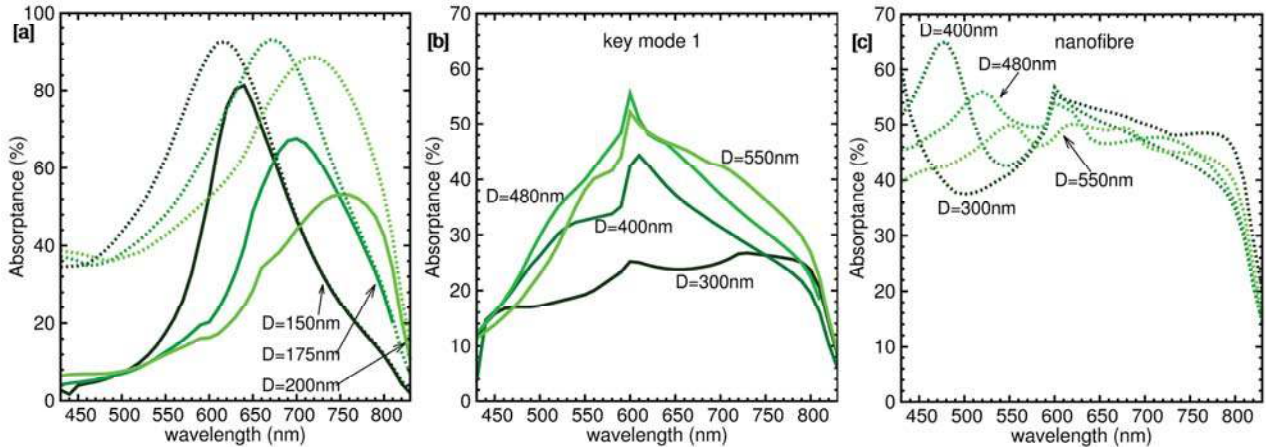


Fig. 7. Absorptance of the key optically guided mode 1 (solid line) and of the ZnO/CdTe nano-fibre arrays (dotted line) for the set of geometrical dimensions B (i.e.,  $P = 600$  nm and different values of  $D$ ). (a) For  $D = 150, 175, 200$  nm and (b-c) for  $D = 300, 400, 480, 550$  nm.

For  $D > 200$  nm, a few key optically guided modes occur as seen in Table 1. For  $D = 300$  nm, the absorptance of the key optically guided mode 1 gets broader as compared with  $D = 200$  nm and covers the visible spectrum ( $430 \text{ nm} < \lambda < 800 \text{ nm}$ ) as seen in Fig. 7(b). Its intensity is however small (about 20%) and the configuration leads to a relatively small absorptance of about 45% for the ZnO/CdTe nano-fibre (Fig. 7(c)). As seen in Fig. 7(b), the key optically guided mode 1 exhibits a sharp absorption peak at  $\lambda = 600$  nm for  $P = 600$  nm. Interestingly, the peak vanishes when  $P$  is changed, suggesting that the key optically guided mode is strongly interacting with the NW arrangement. For  $D > 200$  nm, the absorptance of the key optically guided mode 1 does not fit the absorptance of the ZnO/CdTe nano-fibre

owing to the optical multimode configurations. A detailed key optically guided mode analysis is thus performed for  $D = 480$  nm, in order to elucidate the contribution of the key optically guided modes on the absorptance of the ZnO/CdTe nano-fibre.

### 3.2.2. Study of the geometrical dimensions leading to Max 2

The geometrical dimensions B with  $D = 480$  nm corresponding to Max 2 (Fig. 2(b)) is further studied, in order to quantify the coupling and electric field distribution factors associated with this optical multimode configuration. The characteristics of the four key optically guided modes determined in the wavelength ranging from 430 to 830 nm are reported in Fig. 8. As regards the key optically guided mode 1, the evolution of both  $\rho_y$  and  $\rho_x$  as seen in Fig. 8(b) is similar to the case of the optimal geometrical dimensions ( $D = 200$  and  $P = 350$  nm in Fig. 5(b)).  $\rho_y$  (resp.  $\rho_x$ ) decreases from 56% (resp. 24%) at  $\lambda = 430$  nm to about 14% (resp. 9%)  $\lambda = 830$  nm. The decrease in the confinement of  $E_x$  in the absorbing shell is also shown in Fig. 8(d).

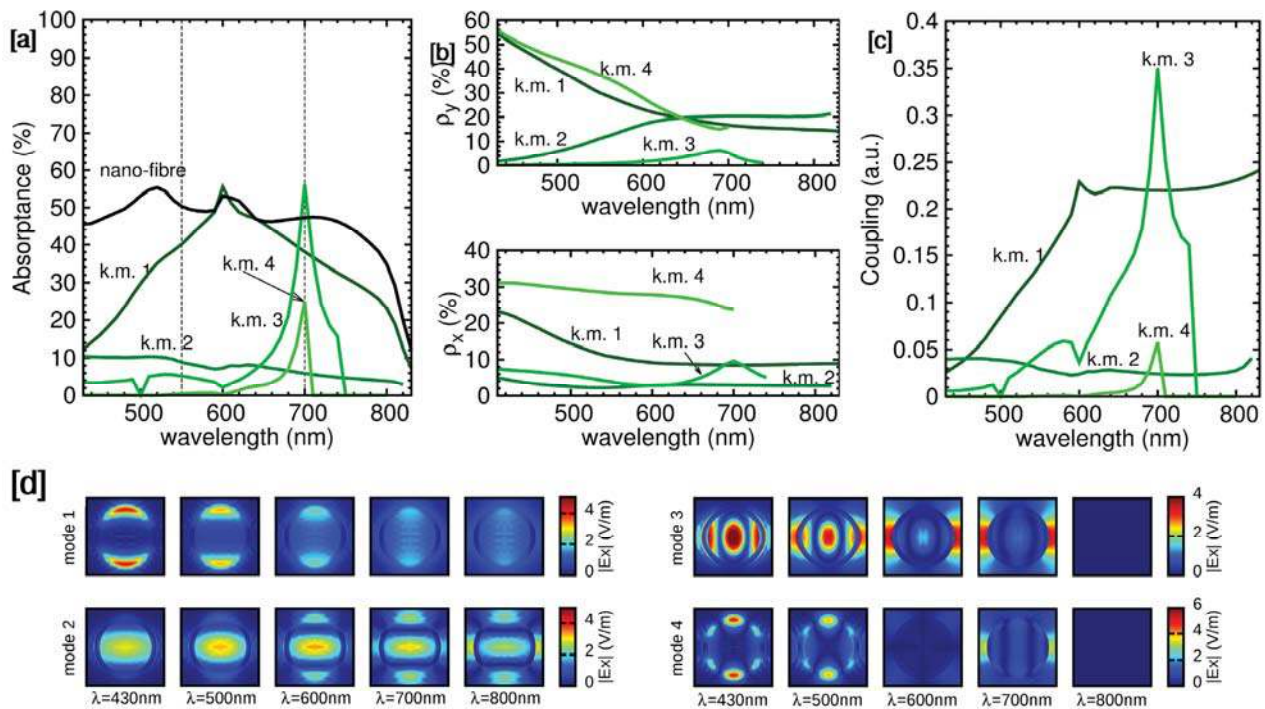


Fig. 8. Characteristics of the key optically guided modes found for the geometrical dimensions with  $D = 480$  nm and  $P = 600$  nm. (a) Absorptance versus wavelength for the key optically guided modes (k.m.) and for the ZnO/CdTe nano-fibre array. (b) Electric field distribution factors  $\rho_x$  and  $\rho_y$  versus wavelength and (c) coupling factor of the key optically guided modes versus wavelength. (d) Maps of the module of the electric field  $E_x$  for the key optically guided modes represented for various wavelengths.

The coupling factor of the key optically guided mode 1 as presented in Fig. 8(c) linearly increases with wavelength from almost zero at 430 nm to its maximum value of about 0.22 at 600 nm and then saturates. Indeed, the intensity of  $E_x$  (Fig. 8(d)) decreases as wavelength is increased, favoring the spatial overlap with the incident plane wave [32] and hence the coupling factor. Since the electric field is as confined as in the case of the optimal geometrical dimensions, the smaller absorptance ( $A = 55\%$  at  $\lambda = 600$  nm, Fig. 8(a), vs  $A = 68\%$  at  $\lambda = 700$  nm, Fig. 5(a)) is ascribed to the smaller coupling factor.

The key optically guided mode 2 does not exhibit large absorptance ( $A < 10\%$ ) for the whole set of geometrical dimensions B. This is mainly due to the small coupling factor of about 0.05 for Max 2. In contrast,  $\rho_x$  and  $\rho_y$  with values of 4 and 20% are relatively large for Max 2.

As  $D$  is increased, the cutoff wavelengths of the key optically guided modes 3 and 4 increase and reach the long wavelength regime for  $D = 480$  nm (see Table 1). For  $D = 480$

nm, the key optically guided modes 3 and 4 have a significant coupling factor around  $\lambda = 700$  nm with  $\rho_x$  and  $\rho_y$  larger than 8% and 10%, respectively. Therefore, they strongly absorb at 700 nm ( $A = 56$  and 25% for the key optically guided modes 3 and 4, respectively) as seen in Fig. 8(a). The strong absorption at  $\lambda = 700$  nm is likely originating from strong interaction with the NW arrangement since the electric field amplitude is significant outside the ZnO/CdTe NW, as seen in Fig. 8(d). The key optically guided modes 3 and 4 contribute to the total absorption of the ZnO/CdTe nano-fibre array in addition to the key optically guided mode 1. The geometrical dimensions with  $D = 480$  nm thus lead to Max 2. However, it is worth noticing that the absorptance of the ZnO/CdTe nano-fibre array is significantly lower for Max 2 ( $A \sim 45\%$ ) than for the optimal geometrical dimensions ( $A \sim 75\%$ , Fig. 5(a)).

In summary, the set of geometrical dimensions B exhibits two maxima: Max 1 and Max 2. Max 1 is found to originate from one key optically guided mode located in the long wavelength regime, as in the case of the set of geometrical dimensions A. In contrast, Max 2 can be explained by the significant absorption of the broad and large key optically guided mode 1. The key optically guided mode 1 is, to a lesser extent, assisted by the absorption of three other key optically guided modes, which can be well-coupled with the NW arrangement for specific wavelengths.

#### 4. Conclusion

The physical mechanisms responsible for light absorption have been numerically investigated by 3D RCWA in a novel class of core shell NW-based solar cells involving ZnO NWs covered with a semiconducting absorbing shell (i.e. the so-called ETA solar cells). Thanks to RCWA which gives access to the modal behaviour of the structure, the absorption has been analysed through optical modes for two representative sets of geometrical dimensions. The first set of geometrical dimensions with a constant  $D$  of 200 nm and varying  $P$  has been investigated in order to study the absorptance originating from individual NW effects through optically guided modes and from NW arrangement effects through optical modes efficiently coupled with the incident light and interacting with nearby NWs (i.e., diffraction processes). It is shown that the absorptance is driven by one key optically guided mode in the long wavelength regime ( $\lambda > 700$  nm). NW arrays arranged with a period of 350 nm probably benefit from diffraction processes, enhancing the absorptance in the short wavelength regime ( $\lambda < 550$  nm). The optimal geometrical dimensions (i.e.  $D = 200$  nm and  $P = 350$  nm) thus probably arise from a trade-off between efficient diffraction process coming from NW arrangement effects and the large absorptance of one key optically guided mode in individual NWs. Owing to these two efficient absorption mechanisms, Fabry-Perot resonances between the top and the bottom of the NW arrays can only improve the light absorption by less than 10%. It is expected that these absorption mechanisms also lead to the optimal geometrical dimensions in case of NW arrays made of other direct band gap materials because of their high optical absorption coefficient.

The second set of dimensions with a constant large  $P$  and varying  $D$  has been used to investigate the absorptance of individual NWs with single and multiple key optically guided modes. The optical multimode configuration with  $D = 480$  nm exhibits a local maximum related to the relatively broad and large absorptance of the key optically guided mode 1, which is assisted to a lesser extent by the absorption of three other key optically guided modes. Although, optical multimode configurations with large diameters are not optimal in case of ZnO/CdTe NW arrays, they may be beneficial for indirect band gap materials such as Si.

It should be noted that the general physical mechanisms described for light absorption in ZnO/CdTe core shell NW arrays can apply to other semiconducting absorbing shells made of direct band gap materials such as CdSe, CIS or CdS for instance. However, the details related to the optimal geometrical dimensions and wavelength regime may slightly be affected. The optical potentialities of ZnO NWs covered with a semiconducting absorbing shell are therefore high, revealing the large interest of these new heterojunctions for the field of photovoltaics as ETA solar cells.

## Appendix A: convergence of the RCWA simulator

The 3D RCWA optical tool developed at IMEP-LAHC laboratory takes into account the symmetry and normal field implementations [29] to ensure fast and efficient convergence. The symmetry implementation is able to decrease the matrix size by a factor of 4, therefore reducing the computation time. The normal field implementation is used to express continuous quantities with Fourier expansions [36] and thus ensures an efficient convergence.

The ideal  $J_{sc}$  has been calculated for the ZnO/CdTe core shell NW arrays with  $P = 350$  nm and  $D = 210$  nm for various truncated order (harmonic number) of the two dimensional Fourier series of the fields. The relative error of the ideal  $J_{sc}$  with respect to the case with 25x25 harmonics (25 harmonics for both Fourier series) is reported in Fig. 9. It is shown that as the harmonic number increases, the relative error tends to zero. The relative error is smaller than 0.1% for 10x10 harmonics and thus was considered as sufficiently accurate.

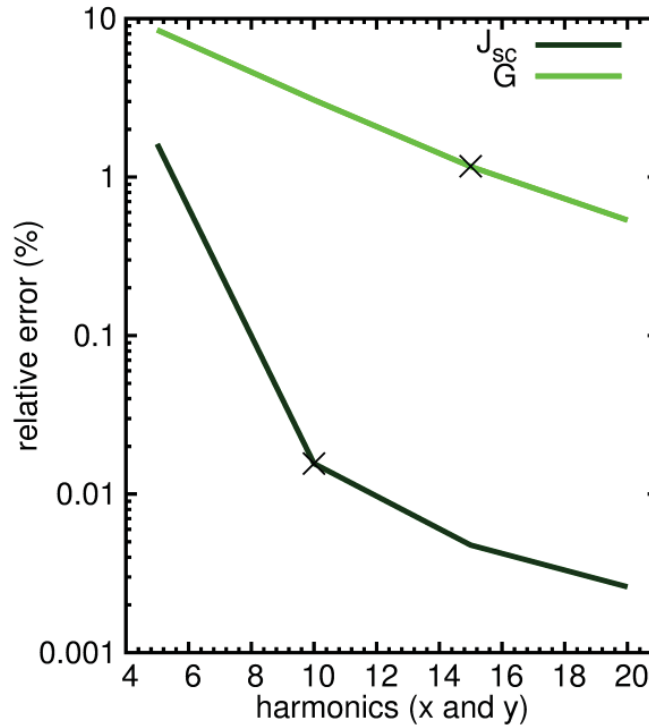


Fig. 9. Convergence of both the ideal  $J_{sc}$  and the surface integrated generation rate  $G$  versus the harmonic number for both Fourier series. It has been calculated for the ZnO/CdTe NW arrays with  $P = 350$  nm and  $D = 210$  nm. The reference value is calculated with 25x25 harmonics.

The radial generation rate is computed for various harmonic numbers and subsequently integrated numerically over the  $r$ - $z$  plane with step size of 1 and 0.5 nm along the  $r$  and  $z$  directions, respectively. The relative error of the surface integrated radial generation rate for 15x15 harmonics with respect to that calculated for 25x25 harmonics is smaller than 2% as shown in Fig. 9. Therefore, the generation rate was computed with 15x15 harmonics.

## Appendix B: optically guided mode absorptance calculation

The absorptance of a given optically guided mode over a given depth  $L$  is computed with Eq. (6) assuming that the NW has a semi-infinite length.

$$P_{\text{absorbed}} = |Sw|^2 P_{\text{modal}} [1 - \exp(-2\Im(\beta)L)], \quad (6)$$

where  $|Sw|^2$  is the excitation mode amplitude (or coupling factor), which depends on the mode normalisation. In fact, the excitation mode amplitude is determined by ensuring the continuity of the transverse electric and magnetic fields at each interface between two consecutive layers.  $P_{\text{modal}}$  is the spatial integral of the Poynting vector for a given mode.  $\beta$  is the complex propagation constant of the optically guided mode. The absorbed power is given by Eq. (6) if the mode is single and gives a good metric to distinguish the optically guided

modes. The related absorptance can be deduced by dividing the absorbed power by the total light intensity impinging the device. If the absorptance of the optically guided mode is larger than 1%, the mode is referred as a key optically guided mode.

### Appendix C: generation rate calculation

The procedure used to calculate the generation rate is described in this appendix. The 3D generation rate is calculated with Eq. (7).

$$G(r, \theta, z, \lambda) = \frac{\pi \cdot \Im[\varepsilon(r, \theta, z, \lambda)] \cdot |E(r, \theta, z, \lambda)|^2}{h}, \quad (7)$$

where  $\varepsilon$  and  $E$  are the permittivity and the electric field, respectively.  $r$ ,  $\theta$  and  $z$  are the variables of the cylindrical coordinate system.

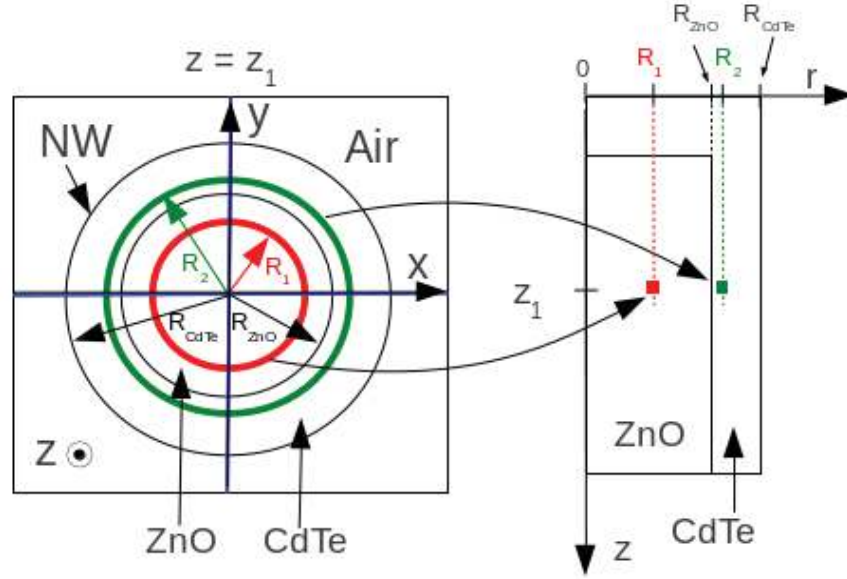


Fig. 10. Procedure to compute the radial generation rate map. 3D generation rate is averaged over a circle perimeter to determine the radial generation rate.

The  $r$ - $z$  generation rate calculation is summed up in Fig. 10. Figure 10 shows a  $x$ - $y$  cross section of the structure at a given depth  $z$ . For each radius  $R$ , the generation rate is averaged over a circle perimeter. Figure 10 shows the circle perimeter for two points, one in the ZnO NW core and the other in the CdTe shell. By following this procedure for each radius  $r$  and depth  $z$ , the radial ( $r$ - $z$  plane) generation rate can be determined [33] via Eq. (8).

$$G(r, z, \lambda) = \frac{1}{2\pi} \int_{\theta=0}^{2\pi} G(r, \theta, z, \lambda) d\theta, \quad (8)$$

Using the result of Eq. (8), the map of the generation rate weighted by the solar irradiance can also be computed:

$$G(r, z) = \int_{\lambda} \frac{I_{AM1.5g}(\lambda)}{I_{incident}} G(r, z, \lambda) d\lambda, \quad (9)$$

where  $I_{incident}$  is the light intensity shining on the structure.

### Acknowledgments

This work has been partially supported by the European commission FP7 program within the framework Network of Excellence Nanofunction under a grant agreement no. 257375. The authors also acknowledge the financial support of Grenoble-INP via a Bonus Qualité Recherche grant through the project CELESTE.